Copper-iron ternary metal fluorides from multi-metallic template fluorination and their first use as cathode in solid state Li-batteries

Fabien Eveillard, Fabrice Leroux, Nicolas Batisse, Diane Delbègue, Katia Guérin

Copper-iron ternary metal fluorides from multi-metallic template fluorination and their first use as cathode in solid state Li-batteries

Fabien Eveillard[a,b], Fabrice Leroux[b*], Nicolas Batisse[b], Diane Delbègue[a], Katia Guérin[b*]

[a] Université Clermont Auvergne, CNRS, Institut de Chimie de Clermont-Ferrand, F-63000 Clermont Ferrand, France.

[b] Centre National des Etudes Spatiales, 18 avenue Edouard Belin 31 401 Toulouse Cedex 9, France

Abstract

Conversion cathodes such as metal fluorides are particularly interesting for their theoretical capacities up to 711 mAh/g when used in Li-ion batteries. However, they generally suffer from high hysteresis and/or poor cyclability. To overcome these problems, ternary metal fluorides are being explored to improve electrochemical properties compared to the usual binary fluorides: a polymer electrolyte membrane is also used to avoid undesirable cathode-electrolyte reactions and to assess the compatibility of such cathode materials with All Solid State Batteries (ASSB). Among the multi-metallic models, copper hexacyanoferrate $Cu_3[Fe(CN)_6]_2.nH_2O$ from the Prussian blue analogue family (PBA), is fluorinated under pure fluorine gas at selected temperatures according to preliminary thermogravimetric mass spectrometry analyses. Using X-ray absorption spectroscopy and diffraction, an inverse perovskite structure $[Cu(H_2O)_4]_3.(FeF_6)_2$ is identified at a fluorination temperature of 140 °C and an intimate mixture of CuF_2 and FeF_3 is formed at 350 °C. The cyclic voltammogram of the latter compared to that of a ball-milled sample of similar composition CuF_2/FeF_3 highlights the advantages of MMTF multi-metallic template fluorination for electrochemical properties, interpreted by the high level of homogeneous dispersion of the redox centres obtained with this method compared to the mechanical milling reference evaluated by SEM. The fluorides are also found to be compatible with the commercial solid polymer electrolyte membrane PEO-LiTFSI (Poly Ethylene Oxide

impregnated with Lithium bis(trifluoromethanesulfonyl)imide), underlining the suitability of the MMTF-prepared cathodes for use in the ASSB.

Keywords

MultiMetallic Template; Prussian Blue Analogues ; Solid Gas Fluorination ; ASSB ; Cathode materials ; Cyclic Voltammetry ; Solid Polymer Electrolyte

1. Introduction

Lithium-ion batteries are key components for new portable applications. However, their performance is limited by cathode materials, as evidenced by Li-rich cathodes and Li-(NiMnCo)O_2 (NMC) materials with a specific capacity of less than 280 mAh.g^{-1} in commercial cells to date (Rozier & Tarascon, 2015).

Many materials are relevant candidates to improve this capacity such as conversion type cathodes (Nitta et al., 2015) even if it implies lithium metal as anode and the subsequent challenge to overcome the formation of dendrites. Among them, metal fluorides are particularly interesting (Hayner et al., 2012; Lemoine et al., 2021; Lemoine, Zhang, Dambournet, et al., 2019; Lemoine, Zhang, Grenèche, et al., 2019) such as FeF_3 with a theoretical capacity of 712 mAh.g^{-1} for three exchanged electrons at a voltage of 2.74 V *vs*. Li^+/Li or CuF_2 with a theoretical capacity of 528 mAh.g^{-1} at a high voltage of 3.55 V *vs*. Li^+/Li. In general, MF metal fluorides suffer from relatively high voltage hysteresis and cyclability problems related to the dramatic volume change involved in the conversion step resulting from the transformation of MF species in a LiF + M matrix (Wu et al., 2020). In this article, different solutions existing in the literature are coupled to evaluate their electrochemical properties and to show some ways to solve problems encountered with binary fluorides.

First, to avoid side reactions of the active material with organic electrolytes such as dissolution of metal fluorides during cycling often encountered, conventional organic electrolytes can be replaced by solid electrolytes. Indeed, promising results have already been obtained by Huang et al. (Huang et al., 2019) for a sample of FeF_2 coupled to a PEO/LiTFSI (Poly Ethylene Oxide impregnated with Lithium bis(trifluoromethanesulfonyl)imide) solid polymer electrolyte (SPE) at 50 °C for 300 cycles. SPEs could therefore allow the use of CuF_2 as cathodes without the problems associated with its reactivity toward conventional organic electrolytes. Improvements in the hysteresis are

also observed by Huang et al. most likely by minimizing the volume expansion that occurs during the conversion of metal fluorides.

Secondly, with the observation that ternary metal fluorides such as $Cu_xNi_{1-x}F_2$ (Villa et al., 2019) and $Cu_yFe_{1-y}F_2$ (F. Wang et al., 2015) are effective in improving electrochemical properties, a suitable ternary composition is required. Indeed, the aim is to combine the advantages of individual binary fluorides while buffering volume expansions that can potentially improve cyclability and minimize voltage hysteresis. However, such ternary systems are prepared by mechanical milling or aqueous fluorination with HF hydrofluoric acid, both of which are difficult to scale up or inhomogeneous process.

An innovative method explored in this work is to use a multi-metallic template to prepare ternary metal fluorides by pure gaseous molecular fluorination. Such possibility was demonstrated by Lemoine et al. (Lemoine et al., 2021) via the gaseous fluorination of ammonium multimetallic fluoride precursors. They observed the formation of multimetallic pyrochlore fluorides via a topotactic oxidation mechanism.

In our case, we chose copper hexacyanoferrate, a copper-iron based compound of the Prussian Blue Analogues (PBAs) family, is chosen here as a model for its different properties to prepare a $Cu_xFe_yF_z$ composite by gaseous fluorination. Iron and copper were chosen based on the electrochemical properties of FeF_3 and CuF_2 for its high capacity and high voltage, respectively: both properties could therefore be recovered by mixing these compounds in a unique product. As for PBAs, these compounds can be easily prepared by co-precipitation in large quantities, allowing for an industrial scale application.

PBAs are widely studied for their open structures and cation exchange properties used for different purposes such as electrochromism, ion detection or electrocatalysis (de Tacconi et al., 2003) but also as electrode materials(D. Wang et al., 2021; Wessells et al., 2011). PBAs are also used as calcination templates to easily obtain a wide range of oxides with unique morphologies (Ju et al., 2021; Li et al., 2019; Zhang et al., 2012, 2013). Indeed, CuPBA framework with the formula $Cu_3[Fe(CN)_6]_2.xH_2O$ integrates the transition metal centers of electrochemical interest, iron and copper, in a face-centered cubic structure and offer the possibility to form multimetallic oxides by calcination under air as seen in literature (Cheng et al., 2019). In line with this observation, by switching the calcination atmosphere to gaseous molecular fluorine, original structures and morphologies of mixed fluorides could therefore be obtained using solid gas fluorination as a scalable method for industrial applications. Particular

attention is given to understanding the mechanism of fluorine addition on CuPBA as a function of process temperature. To date, few works are reported on PBAs fluorination using pure fluorine gas: these publications offer insights on the relevance of such process to obtain original fluorinated structures. For example, Gu et al. (Gu et al., 2021) studied the effect of fluorination on a CoFe PBA framework at different temperatures but using NH_4F fluorinating agent: they observed the possibility to either maintain the original template structure at 150 °C or to prepare a mix of corresponding fluorides ($KCoF_3$ and $KFeF_3$) at 250 °C and above. They also assessed a porosity enhancement, thus highlighting the possibility to control both the structure and the porosity of the fluorination product. This double feature offered by the control of fluorination temperature is highly enticing for the preparation of cathode materials with different electrochemical properties, as these are linked to both characteristics.

Beforehand, the fluorination temperatures are selected based on thermogravimetric measurements coupled with evolved gas analysis by mass spectrometry (MS-TGA) of CuPBA prior to an in-depth structural characterization investigated using X-ray absorption spectroscopy (XAS) and diffraction (XRD). The structural change is followed as a function of fluorination temperature, reporting the near-edge structure as well as a qualitative analysis of the Fourier transforms at both transition metal absorption K edges.

The electrochemical behavior is evaluated in all solid-state battery (ASSB) set-up using PEO/LiTFSI as a solid polymer electrolyte (SPE). The insertion and conversion mechanisms are scrutinized using cyclic voltammetry (CV) at slow sweeping rate (20 $\mu V\ s^{-1}$) over a wide-open potential window (50 mV to 4.1 V *vs*. Li^+/Li). The shape of CVs is compared to that of a ball-milled sample with equivalent CuF_2/FeF_3 chemical composition to the one identified in CuPBA after fluorination at 350 °C. Finally, the voltage as a function of the capacity of each candidate is recorded in galvanostatic-mode.

The strategy applied in this article called MultiMetallic Template Fluorination (MMTF) focuses on the preliminary study of the thermal behavior of the sample and can eventually be generalized to other multi-metal models to obtain a wide range of fluorinated products.

2. Experimental section

2.1. Material synthesis and fluorination

Synthesis of 10g of the copper-based Prussian Blue Analogue (CuPBA) with the formula $Cu_3[Fe(CN)_6]_2$. xH_2O was prepared by the classical co-precipitation protocol, adding 3 molar equivalents of $CuCl_2.2H_2O$ to 2 molar equivalents of $K_3Fe(CN)_6$ in distilled water. Both reagents were of grade ≥99% and used without prior purification. A precipitate immediately began to form: magnetic stirring was kept for a few minutes until the solution was homogenized. The product was immediately centrifuged and washed several times with distilled water. The product was recovered, after drying in an oven for 24 hours at 50°C and manual mixing, as a fine dark green powder and used as such for fluorination and characterizations.

Fluorinations were performed in dedicated equipment using special handling procedures (Batisse et al., 2011). Gaseous fluorine was purchased from Solvay Fluor (purity 98-99% v/v with HF max. 0.5% v/v and other gases, mainly O_2/N_2 at about 0.5% v/v). A cylindrical nickel reactor of approximately 50 cm in length and with a volume of about 1 L was used for the reaction. Heating was ensured by a horizontal tube furnace surrounding the reactor, with a homogeneous temperature range of approximately 10 cm. All samples were set in a 10 cm long passivated nickel boat. 200 mg sample was first degassed in the RT oven with nitrogen for 30 minutes to clean it. Then, the sample was heated: a ramp of 5°C min^{-1} was applied until the desired fluorination temperature was reached. The nitrogen flow was cut and fluorine was injected into the reactor: the temperature and fluorine gas flow were kept constant for three hours. A cooling quench was performed and nitrogen was injected when the temperature fell below 100°C to remove any remaining fluorine gas in the oven. The products were extracted and stored under Argon in a glove box to avoid unwanted degradation by air. Each product has been made 3 times and the same XRD and TGA validate the reproducibility of the process.

2.2. Structural characterization

X-ray diffraction (XRD) experiments were carried out on a Panalytical X-Pert Pro diffractometer equipped with a Cu Kα1 source diffracted beam monochromator and a linear X'celerator detector using a home-made measuring cell that allows data to be collected under a static inert argon atmosphere. The counting time was 108 seconds and the angle step size was 0.0167° in the 2-theta 10-80° range. The fittings were performed using the Profex software, developed by Döbelin et al. (Doebelin & Kleeberg, 2015)

X-ray absorption spectroscopy (XAS) measurements of the K-edge of copper and iron were performed at 80K in transmission mode on the SAMBA (Briois et al., 2011) beamline of the SOLEIL Synchrotron (Gif-sur-Yvette, France). A sagittally focusing Si (220) monochromator was used. The intensity of the monochromatic X-ray beam was measured by the detectors of the ionization chambers. The samples were prepared by dilution with cellulose and pressed into pellets. Any contact of the fluorinated products with ambient air during measurements was avoided by placing the pellet in Kapton. 3 successive scans were performed to ensure reproducibility of the measurements. Equidistant energy steps of 0.5 eV were used. Calibration was established by simultaneous absorption measurements of Fe and Cu metal foils. The data were averaged and normalized using ATHENA software (Ravel & Newville, 2005). The Pseudo Radial Distribution (PRD) presented is not corrected for phase shift as the product composition is rather inhomogeneous. The ThermoGravimetric analyses were performed on the Netzsch STA F3 Jupiter. Three preliminary vacuum cycles were performed to clean the sample chamber before starting the measurements. The sample was heated at 10°C min^{-1} in the range RT-600°C either under Helium at 70 $ml.min^{-1}$ or dry air at 70 $ml.min^{-1}$ (80/20% v.v N_2/O_2). An average of 20 mg of the sample was placed in the alumina crucible with a lid in the glove box in a special disposal to avoid contact with ambient air for the transfer to the TG sample chamber. The analysis of the evolved gases was processed by mass spectrometry (Netzsch Aeolos Quadro) coupled to the STA (Simultaneous Thermal Analyzer). The main signals of the evolved gases detected by MS were superimposed but only for qualitative comparison.

The different samples were characterized by Scanning Electron Microscopy (ZEISS Supra SEM operating at 3 kV).

2.3. Electrochemical characterization

The electrochemical properties of the different products were evaluated at 60°C in order to obtain optimal cycling and more particularly in order to favor lithium diffusion in the solid electrolyte used. Before the preparation of the electrode, the product (MF) was mechanically milled with acetylene black (AB) to improve the conductivity of the electrode in a weight ratio MF/AB: 50/50 for 6h at 350 rpm in a planetary ball milling. All subsequent steps were performed in an argon-filled glove box. The cathode material was prepared by dispersing the active material (FeF_3-AB composite) and PVDF as a binding agent in a weight ratio of 45:45:10 in propylene carbonate solvent until a homogeneous slurry was obtained. After drying at 80°C, the working electrode consisted of a stainless-steel grid (14 mm diam., 0.2 mm thickness) with a deposit of 4-6 mg (1.8-2.7 mg of active mass). The electrochemical cell was a

two-electrode coin cell (CR2032). A high purity lithium metal disk (1 mm thick - Aldrich) was used as negative and reference electrodes. Consequently, all voltage values mentioned here are expressed vs Li^+/Li. As electrolyte, a 200 µm membrane of a PEO-LiTFSI mixture (H-Polymer, NEI Corporation) was placed between the cathode and lithium. This commercial powder was solubilized in pure acetonitrile in 14% wt. The obtained solution was stirred until complete dissolution and then poured into a PTFE dish. Mass calculations were made in order to obtain a 200 µm thick membrane with good mechanical properties. An amorphous polymer is obtained at RT with a glass transition temperature below 0 °C and a claimed ionic conductivity of 5.10^{-5} S/cm at RT.

Electrochemical measurements were carried out on a VMP3 or a BCS Biologic instrument. Relaxation was performed for at least 5 h until the open circuit voltage (OCV) stabilized. Almost 3 coin cells were made for each product in order to insure reproducibility of the results.

Cyclic voltammetry was performed at 0.02 mV s^{-1} in the 0.05-4.1 V range.

Galvanostatic experiments were carried out in the 1-4.1 V with a 10/2 mA.g^{-1} of active mass current density for discharge/charge, respectively.

3. Results and Discussion

3.1. Characterization of non-fluorinated CuPBA structure

An easy and scalable co-precipitation between the two salts $CuCl_2.2H_2O$ and $K_3Fe(CN)_6$ in aqueous medium is known to produce the Prussian Blue Analogue (PBA) copper hexa-cyanoferrate referred here as CuPBA (Ojwang et al., 2016). The phase identification of the as-prepared CuPBA performed by X-ray diffraction is displayed in Figure 1. The X-ray pattern of the well-crystallized product agrees with the reference structure of CuPBA from the ICSD database (#252537).

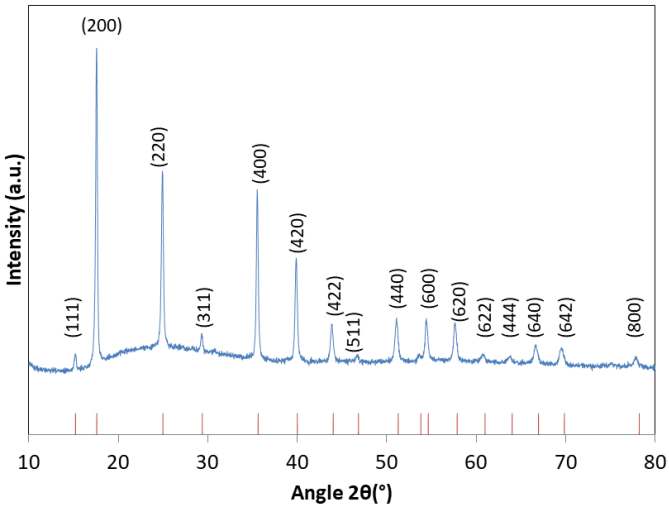

Figure 1: X-ray diffractogram of the as-prepared CuPBA, the red bars represent the ICSD reference of CuPBA #252537

The cubic face centered crystal structure is depicted in space group Fm-3m with Fe^{3+} ions located in the O_h sites surrounded by the six cyanide ligands across the carbon atoms, while Cu^{2+} ions are linked to the nitrogen atoms. The whole framework has an open structure allowing the insertion of a wide range of alkali cations. In their absence, the empty spaces are occupied by zeolite-type water molecules, and ⅓ of $Fe(CN)_6^{3-}$ groups are missing to counterbalance the excess of positive charge, leading to randomly located vacancies in the CuPBA structure.

Coordination water molecules complete the filling of atomic positions, resulting in a mixed environment for the copper ions CuN_6 and CuN_4O_2 as shown in ESI.

3.2. Thermal behavior of CuPBA

To finely tune the fluorination temperature and to select the appropriate temperatures in specific loss events, TGA-MS analysis is applied to the as-prepared CuPBA in air and in inert He atmosphere. Synthetic air (20% v/v O_2 / 80% v/v N_2) is chosen as the oxidizing atmosphere to give the general trend lines of the thermal behavior of CuPBA during oxidation, as it is not possible to perform TGA under pure fluorine atmosphere. Figure 2 and Figure 3 report the thermograms under air and under He respectively: associated volume evolution of the main identified gases as a function of the mass/charge ratios (m/z) recorded simultaneously up to 450 °C are also added. During heating, TGA-MS analysis allows the separation of three main temperature ranges as shown by the gas evolutions under both atmospheres: zone 1 for T < 170 °C, zone 2 with 170 °C < T < 230 °C and zone 3 with T > 230 °C.

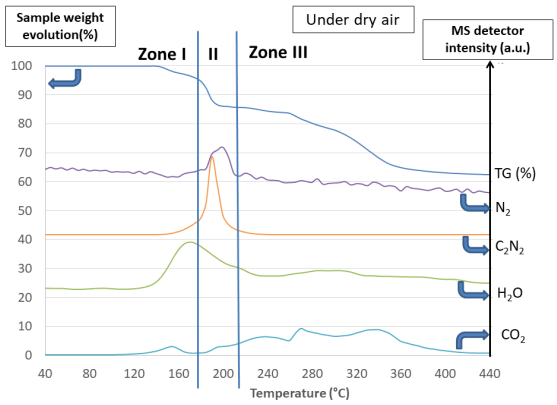

Figure 2: MS coupled TGA of CuPBA sample under dry air at a heating rate of 10 °C min^{-1}

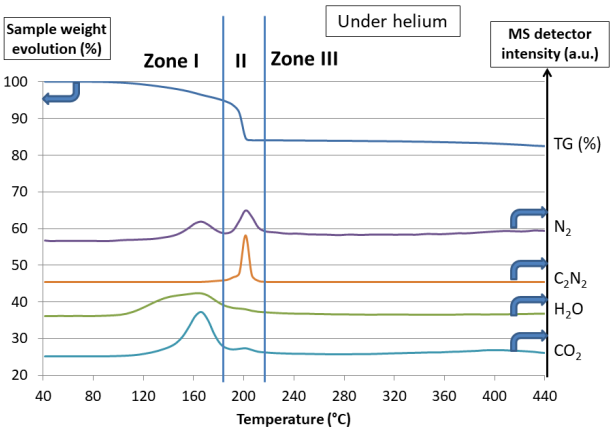

Figure 3: MS coupled TGA of CuPBA sample under He at a heating rate of 10 °C min^{-1}

In both atmospheres, the loss events and associated evolved gas departures that occur in Zones I and II are qualitatively similar. This supports a close thermal behavior in both atmospheres up to 230 °C. This signal is related in both cases to the C_2N_2 signal but also to the H_2O signal as shown by similar characteristics at 160 and 200 °C under helium. This could be related to a gradual degradation of the template structure following the removal of the ligands in both cases, as the coordinating water molecules are also part of the ligands. As for CO_2 and N_2 signals, these are also associated with the departure of the coordination water molecules leading to the destabilization of the PBA template and the removal of a small part of the CN ligands.

In zone III, there is no apparent thermal event under He, whereas the mass loss is largely pronounced under air, corresponding to the formation of oxides with a regular production of off-gas by CO_2.

In more detail for each temperature zone, the first mass loss of about 5 wt% between room temperature and 160 °C corresponds to a departure of H_2O according to the analysis of the gases emitted and detected by the MS in agreement with the literature (Martínez-Garcia et al., 2006).

However, this dehydration process is generally reported to represent about 20% mass loss, much higher than in the present case. This is explained by the preliminary vacuum purge cycle prior to the measurements, causing a partial dehydration of the sample prior to analysis by desorption of weakly bound adsorbed water molecules as well as some zeolite-like water molecules, while strongly bound coordinated water molecules remain after the vacuum treatment. The influence of the vacuum purge cycle on the first weight loss is demonstrated in ESI with supplementary TGA measurements in this area without preliminary vacuum purge. The removal of the coordination

water molecules leads to a partial destabilization of the structure, as shown by the simultaneous production of CO_2 and N_2 resulting from the removal of a small part of CN ligands.

In zone II, a second mass loss is associated with an intense primary signal m/z = 52 and a secondary signal m/z = 26 of similar shape under both atmospheres. Both signals are attributed to C_2N_2 gas and its CN fragment, respectively, and result from the departure of the ligands from the sample, thus inducing thermal degradation of CuPBA (as shown in ESI by XRD). According to the air residues XRD analyses presented in ESI, the CuPBA pristine material is kept in air until 170 °C before a dramatic increase in the C_2N_2 MS signal. This confirms that dehydration tends to destabilize the structure but that the overall structure of the template is still retained in the zone I. At 200 °C in air, the structure is completely lost, confirming that the temperature zone II transforms the multi-metallic template. After 350°C, the residue is less crystallized, but two peaks are indexed to Tenorite, an allotropic form of copper oxide.

Based on the reactive analogy between the oxidizing effect of oxygen molecules in air and molecular fluorine, three fluorination temperatures are selected: 140 °C, 200 °C and 350 °C, each in each identified temperature zone.

3.3. Fluorination mechanism of CuPBA

In the following section and for the rest of the article, the names CuPBA F140, CuPBA F200 and CuPBA F350 represent the products obtained after fluorination of CuPBA at 140, 200 and 350 °C, respectively, with the standard protocol detailed in the Experimental section.

As fluorination is known to induce a drastic change in the local structure, the local environment of the transition metals, iron and copper ions, is investigated by XAS. The near-edge spectrum (XANES) provides information on the oxidation state and coordination number of the absorbing atom, as reported in pioneering works on various transition metals (Belli et al., 1980; Farges et al., 1997; Wilke et al., 2001). From pristine CuPBA, XANES analysis confirms the presence of Fe^{3+} and Cu^{2+} ions, both adopting the local O_h symmetry, albeit slightly distorted in the case of Cu^{2+} environment (ESI). The XAS analysis is carried out as a function of the fluorination temperature. The XANES spectra but also the corresponding Pseudo Radial Distribution (PDR) obtained from its Fourier transform (FT) of the fluorinated samples at Fe K-edge are displayed in Figure 4 and Figure 6 with the fluoride references respectively. The corresponding measurements obtained at Cu K-edge are presented in Figure 5 and Figure 7 respectively.

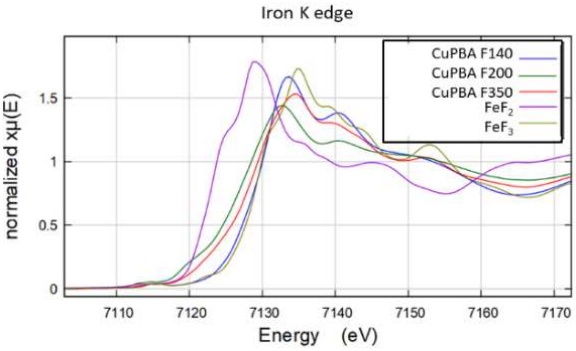

Figure 4 : XANES of fluorinated CuPBA sample at different temperatures and selected references compounds at Fe K-edge

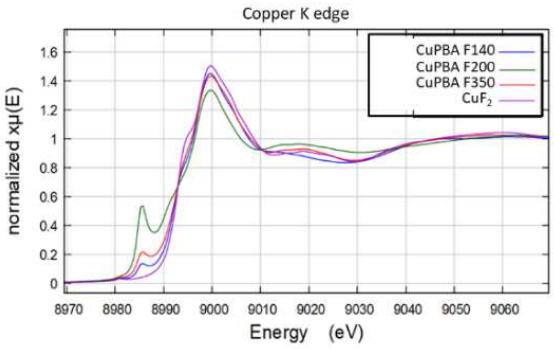

Figure 5 : XANES of fluorinated CuPBA sample at different temperatures and selected references compounds at Fe K-edge

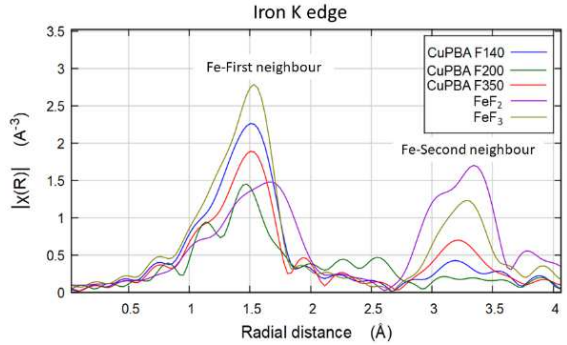

Figure 6 : Pseudo radial distributions (PRD) for fluorinated CuPBA and reference compounds at Fe K-edge

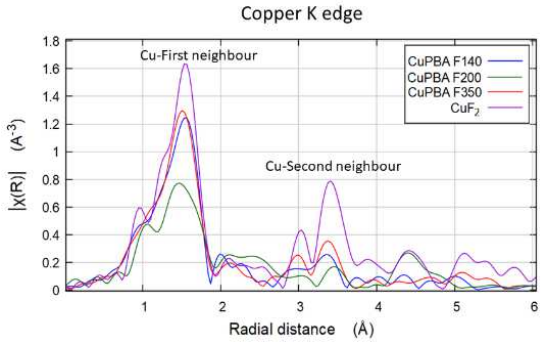

Figure 7 : Pseudo radial distributions (PRD) for fluorinated CuPBA and reference compounds at Fe K-edge

At the Fe K-edge, the XANES spectrum of the fluorinated CuPBA at 350 °C displays the features of the FeF_3 reference, *i.e.* a similar position of the white line (absorption maximum) and an absence of a pre-edge. This indicates the presence of Fe^{3+} iron cations in the O_h site of the sample.

At lower fluorination temperatures, 140 °C and 200 °C, the main transition is observed at lower energy suggesting an average oxidation state for the ferric cations below 3+, as visualized with the variation of the position of the white line as a function of the fluorination temperature presented in ESI. However, it is known that the energy position of the different transitions also depends on the ligand, this being due to the bond strength and its electron donor effect (Wilke et al., 2001).

As the reaction under molecular fluorine is known to be intensively oxidizing, the evolution of the oxidation state of iron cations is prevented even at the lowest treatment temperature. Therefore, the lower energy transitions may result from a change in the ligand rather than a change in the oxidation state, and further analyses are required to confirm the reason for this energy shift. The XANES spectrum at the Cu K-edge for the fluorinated samples exhibits similar features, as expected, since Cu^{2+} is most likely present in all compounds. The main transition remains at a similar energy; however, an intense pre-edge peak is depicted for CuPBA F200, indicating pre-edge energy transitions usually forbidden but allowed here by the local mid-site around low symmetry or highly distorted Cu^{2+} cations. Interestingly, the intensity pre-edge is low for fluorinated CuPBA at 140 °C and 350 °C, while it represents about 40 % of the main transition maximum at 200 °C. As the pronounced pre-edge is usually observed for low symmetry site such as the tetrahedron (Td) or the square plane for Cu cations (Pattrick et al., 1997), it underlines here a severe change occurring locally around the cation Cu^{2+} at 200 °C. According to the TGA-MS analysis in air, the change at 200 °C is explained by the departure of the $(CN)_2$ ligands (Figure 2).

Most likely, a strong site distortion is accompanied by the departure of the ligands at the intermediate temperature of 200°C, as Cu^{2+} cations have to complete the coordination from their vicinity. From the Fourier transforms (FT), the change in the local environment around the two cations is qualitatively observed (Figure 5). The Fourier transforms are not refined due to the change of ligand and phase mixing, but they correspond to the backscattered atoms around the observed cations.

Qualitatively, the shape of the FT around the iron cations is similar between the samples fluorinated at 140 °C, 350 °C and FeF_3, but of lower intensity. For the sample treated at 200 °C, the FT is modified and the first hump is composed of two contributions while the second hump has disappeared. This indicates a strong distortion of the Fe-ligand site with neighbouring atoms at different distances. The second hump is composed of neighbouring Fe-second atoms (most likely another metal atom, Fe-ligand-Fe (or –Cu)), its absence indicates a pronounced amorphization.

For the FT around the copper atoms, the observation is qualitatively similar. For CuPBA after fluorination at 200 °C, the contribution of Cu-first neighbouring atoms is less intense and splits in two contributions, indicating a ligand distance distribution. The first FT split is in agreement with the intense pre-edge while the local site around Cu^{2+} cations is symmetric for the two other temperatures. From a similar interpretation applied to Fe cations, a

discrepancy appears since the fractionation in the absence of pre-edge transition is not due to the site distortion. Most likely, the splitting for Fe FT comes from the presence of two different sites not having the same ligand or a different oxidation state but both symmetrical while it corresponds to a distorted site for Cu FT.

To complete the information at longer coherence lengths, the XRD patterns of the fluorinated samples are studied. Different crystal phases are identified and the resulting fittings for CuPBA F140 and F350 are shown in Figure 8 and Figure 9 respectively while attribution is not possible for CuPBA F200 (shown in ESI). After fluorination at 140 °C, the sample is amorphous, but two crystalline phases are identified. A poorly defined hexagonal tungsten-bronze FeF_3 (HTB-FeF_3) is indexed as well as $[Cu(H_2O)_4]_3.(FeF_6)_2$. The latter exhibits an anti-perovskite structure (or ABX_3 inverse perovskite) as reported by Kummer et al. (Kummer & Babel, 1987). Multi Metallic Template Fluorination MMTF of CuPBA is a possible route to form a structure incorporating both cations at low temperature, as shown by the anti-perovskite crystal structure without the need for HF solution, unlike Kummer's work. After fluorination at 350 °C, the hydrated anti-perovskite phase is degraded resulting in the formation of well-crystallized and intimately mixed phases, CuF_2 and HTB-FeF_3. A fitting stoichiometry of 3 to 2 between CuF_2 and FeF_3, respectively, is found and is similar to the ratio beween Cu and Fe cations in CuPBA of formula $Cu_3[Fe(CN)_6]_2.xH_2O$. This indicates that the reaction at 350 °C is complete and that the CuPBA template irreversibly transforms into CuF_2 and FeF_3.

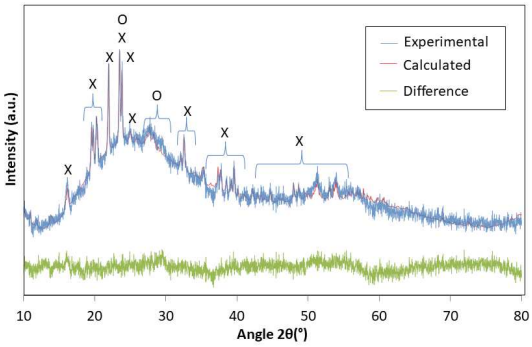

Figure 8 : X-ray diffractograms and phase assignments for CuPBA F140

Symbol - Phase assignment – ICSD code:

O HTB FeF_3 35359

X $[Cu(H_2O)_4]_3.(FeF_6)_2$ 62272

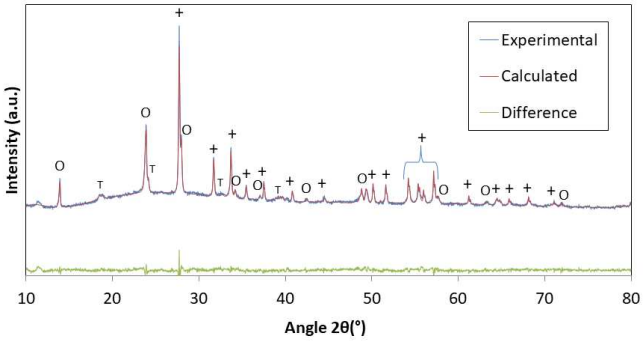

Figure 9 : X-ray diffractograms and phase assignments for CuPBA F350

Symbol - Phase assignment – ICSD code:

+ CuF_2 71833

O HTB FeF_3 35359

The radical change in local order that occurs at 200 °C and in particular for the Cu^{2+} cations can be explained by the phase transformation between $[Cu(H_2O)_4]_3.(FeF_6)_2$ and CuF_2, two phases in which the coordination sphere for the Cu^{2+} cations is different, while the environment around Fe^{3+} cations present in FeF_3 is already in place in the anti-perovskite intermediate phase, as indicated by the Fe and Cu environments in each phase considered and presented in the ESI. It is interesting to note that the coordinating water molecules are further away from the copper atoms in CuPBA (Cu-O of 2.48 Å) than in $[Cu(H_2O)_4]_3.(FeF_6)_2$ (Cu-O between 1.94 and 1.98 Å), while the fluorine atoms are located further in the intermediate phase (between 2.21 and 2.41 Å) bridging with the iron cations. It is also interesting to note that a typical 4 + 2 coordination of copper cations is observed in CuPBA, in CuF_2 as well as in $[Cu(H_2O)_4]_3.(FeF_6)_2$. The shorter Cu-O distance in the inverse perovskite provides a very disruptive binding force for the structure when water molecules leave the structure upon heating and are replaced by fluoride anions. This may explain why the local Cu^{2+} symmetry alternates from a [4 + 2] distorted O_h at 140 °C to a strict *Td* at 200 °C and then to a distorted O_h at 350 °C.

3.4. Thermal analysis of the fluorinated samples

Displayed in Figure 10, the comparison between the TGA analyses of the three fluorinated samples and the original CuPBA under He tends to confirm a profound structural modification of the pristine precursor for the three temperatures as no similarity is found in their thermal evolution behavior. Moreover, a thermal stabilization of the phases is observed when increasing the fluorination temperature: in F-140 and F-200 samples, a significant mass loss (20% at 600°C) is observed whereas less than 5% mass loss is observed in F-350.

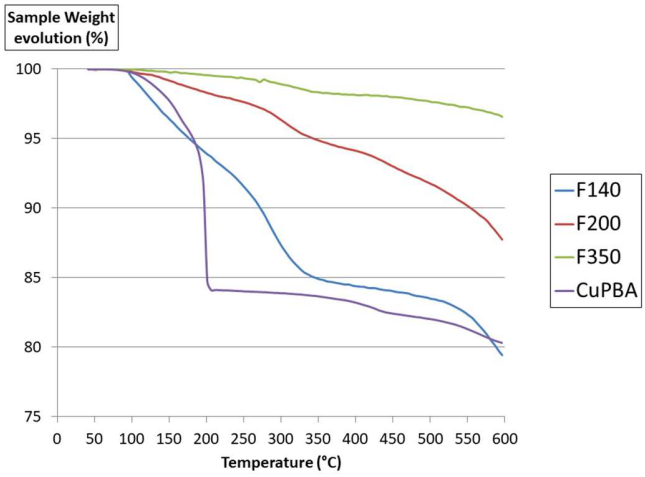

Figure 10: Thermogravimetric analysis of the fluorinated samples CuPBA F-140, -200 and -350 and of the pristine CuPBA sample under Helium ; Heating rate: 10 °C/min

The most striking difference occurs before 300 °C with a pronounced weight loss for the fluorinated samples treated at lower temperatures. Clearly, the F-140 and -200 samples contain water molecules as indicated by XRD with the presence of a hydrated phase $[Cu(H_2O)_4]_3.(FeF_6)_2$, which is less stable than the pure fluorinated compounds. Moreover, this observation can be related to the instability of the FeF_3 and CuF_2 clusters formed. Indeed, as indcated by XRD, a minor FeF_3 phase starts to form at 140 °C. Following the TGA analyses, the FeF_3 domains formed are very small as only two peaks could be assigned to FeF_3 in **Figure 8**. In addition, these domains may have defects that increase their instability and causes them to degrade rapidly with a slight increase in temperature. Therefore, the fluorinated phases formed are only stable at high fluorination temperatures when the CuF_2 and FeF_3 cluster sized are sufficiently large and free of defects to be fully stabilized, while $[Cu(H_2O)_4]_3.(FeF_6)_2$ is completely transformed.

In summary, the FeF_3 and CuF_2 phases are obtained from the fluorination of the CuPBA template at 350 °C. To address the process advantage, CuPBA F350 is compared to the product obtained by planetary ball milling of a 3:2 molar mixture of CuF_2 and FeF_3. The templating approach leads to more crystallized phases than ball milling as shown by the comparative XRD analysis presented in ESI.

3.5. Morphology and elemental distribution in CuPBA F350 compared to ball milling

The impact of the MultiMetallic Template Fluorination on the morphology of CuPBA at high temperatures is assessed by Scanning Electron Microscopy (SEM) performed on the precursor CuPBA and its fluorination product obtained at 350 °C. A comparison of SEM views obtained on CuPBA and CuPBA F350 is presented in ESI. The

CuPBA sample is composed of agglomerated individual particles, mostly cubic-shaped: individual particles diameter ranges from a few nanometers to a few tens nanometers. Interestingly, the fluorination product obtained at 350 °C is mostly composed of agglomerated regularly sized particles with an individual diameter around a few hundreds nanometers even if some bigger agglomerates of a few micrometers are also present as seen in ESI. This characteristic can be linked to the original template crystalline structure. Indeed, copper and iron atoms are placed at fixed distances from each other in the crystalline structure: upon fluorination, we can therefore expect the formation and growth of CuF_2 and FeF_3 domains to occur from the respective atomic positions of copper and iron atoms during MMTF at 350 °C on this template. This enables the formation of homogenized particles.

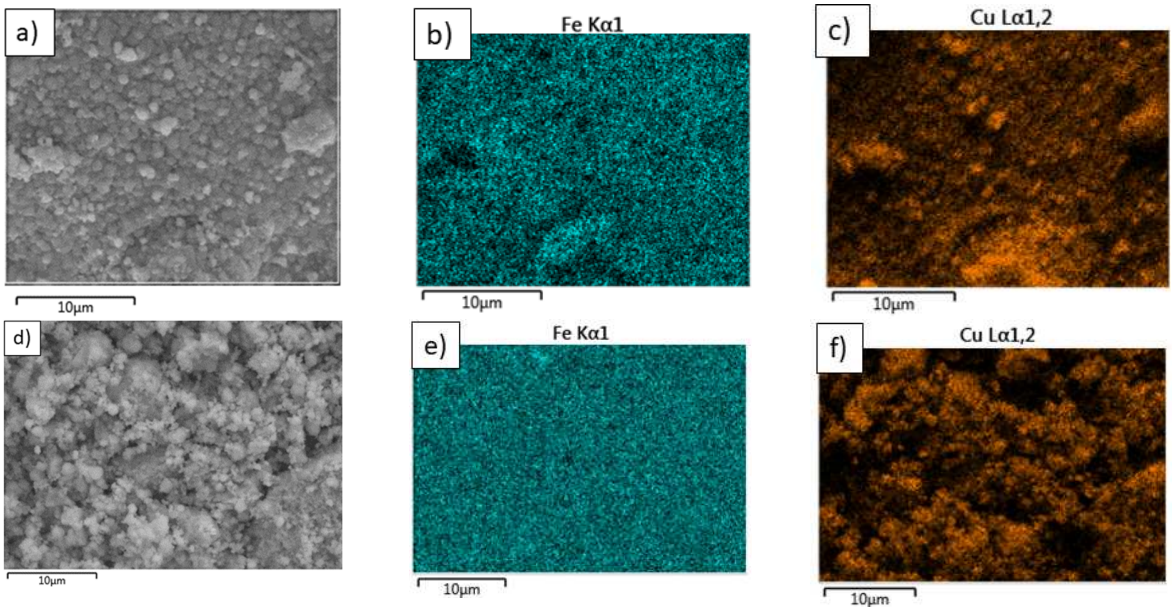

Figure 11: SEM view of a) CuPBA F350 and corresponding EDX mappings of b) iron and c) copper elements SEM view of d) 3 CuF_2/2 FeF_3 mechanical milling product and corresponding EDX mappings of e) iron and f) copper elements

This morphology obtained with MMTF is then compared with the result obtained after ball milling of a 3 CuF_2/2 FeF_3 composition. SEM views and corresponding EDX mappings of iron and copper elements in CuPBA F350 and in this ball milling reference are compared in Figure 11. No clear differences can be found between the dispersion of iron atoms in CuPBA F350 and the ball milling reference. However, the distribution of copper atoms is slightly different between the two samples. In CuPBA F350, these are well dispersed in the entire scan zone, even if more concentrated areas can be found specifically in bigger aggregates. In comparison, copper atoms distribution is more

heterogeneous in the ball milling product, as many zones present a total lack of copper. Additionally, according to the comparison of SEM views, particles diameter is quite heterogeneous in the ball milling product in comparison with CuPBA F350.

We can therefore conclude that CuF_2 domains tends to agglomerate more easily than FeF_3: this tendency is however moderated with MMTF applied to CuPBA than in ball milling thanks to a better initial dispersion of copper atoms in the template, giving a better homogeneous distribution of CuF_2 and FeF_3 domains in CuPBA F350.

3.6. Electrochemical behavior

To determine whether the templating approach is beneficial for the electrochemical response, cyclic voltammetry is recorded to elucidate the successive redox steps in all-solid-state setup using a solid electrolyte membrane. For comparison, the CV is processed on the same active material both in liquid electrolyte (lithium perchlorate $LiClO_4$ dissolved in 1M propylene carbonate) and with the PEO + LiTFSI solid polymer electrolyte (SPE) membrane under the same conditions. As shown by the ESI, the current densities are much higher with the liquid electrolyte than with the solid electrolyte, most probably due to the difference in their ionic conductivity. However, the mechanism is globally conserved as peaks are located in the same areas except at 1V in discharge and 4.1V in charge. Indeed, the peaks at 1V and 4.1V with the liquid electrolyte are ascribed to an undesirable cathode/electrolyte reaction and are not visible with the solid electrolyte confirming that a solid electrolyte inhibits secondary reactions and improves stability at the cost of a loss of ionic conductivity. Consequently, suitable current densities and scan rate are chosen to explore the electrochemical mechanism.

The first and second cycles for each fluorinated sample are displayed in Figure 12 and in Figure 13 respectively. To examine the full electrochemical response, the electrochemical behavior is recorded over a wide voltage window 50 mV to 4.1 V *vs*. Li^+/Li, where the polymer membrane is sufficiently stable as indicated by an additional CV experiment without active material (ESI).

Comparing the mass normalized current, the electrochemical activity varies as CuPBA F350 > CuPBA F140 > CuPBA F200, this for the first two complete cycles. For the first cycle, more pronounced anodic peaks are observed for CuPBA F350, showing the presence of well-defined redox sites in the material at 2.9 and 1.5 V *vs*. Li^+/Li. In contrast, the voltammogram for both CuPBA F-140 and -200 present broad and less intense peaks.

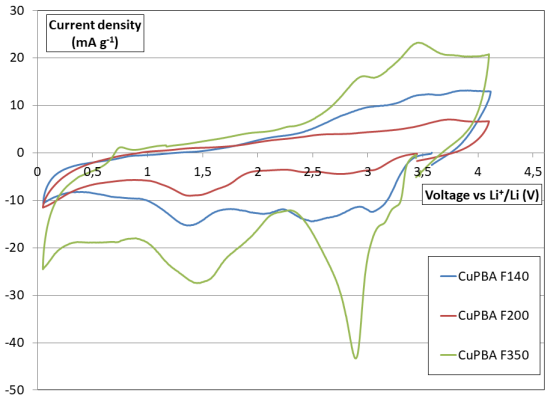

Figure 12: Cyclic voltammetry for the fluorinated samples during 1st cycle Current obtained is corrected by the active mass and the scanning rate is 0.02 mV s^{-1}

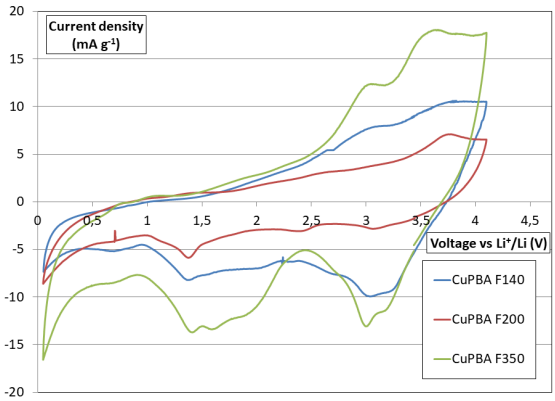

Figure 13: Cyclic voltammetry of the fluorinated samples during 2nd cycle Current obtained is corrected by the active mass and the scanning rate is 0.02 mV s^{-1}

The redox ability of the fluorinated samples is related to the average oxidation state of the two transition cations. It seems difficult to attribute the difference in electrochemical response to the difference in oxidation states, since these are maintained during fluorination to Cu^{2+} and Fe^{3+} in all three materials, as indicated by the material characterization. The difference in electrochemical activity could rather be related to the low electronic conductivity of the anti-perovskite phase present in CuPBA F140 and F200 compared to the fluoride mixture in CuPBA F350, hence inhibiting electrons transfer to the current collector. The redox reaction may also be partially hindered due to the non-accessibility to the redox centers, resulting from a local structure that is not open enough to accommodate Li^+ cations. Indeed, the less defined redox peaks for CuPBA F140 can be explained by the presence of a multi-metallic phase integrating the two redox centers in the same ABX_3 inverse perovskite structure, which is too dense to allow the entry of Li^+ cations. This has the effect of concentrating the redox mainly at the surface of the particles where accessibility is then stopped, resulting in a multi-site or capacitive type response as observed for F-140 and F-200.

To further discriminate the redox centers in CuPBA F350, a theoretical CV response is constructed by summing the response of each redox by cycling CuF_2 and FeF_3 under the same conditions as for the fluorinated samples. The intensity at iso-voltage is added as a function of the cation ratio of 3:2. As before, a 3 CuF_2 /2 FeF_3 composite

prepared by mechanical milling is then compared to the theoretical response to observe whether ball milling leads to a simple addition of the individual electrochemical response of the two materials or whether synergistic effects emerge (shown in ESI).

The voltammogram of the sample obtained by ball milling is compared to CuPBA F350 in Figure 14 and Figure 15 for the first and second cycle respectively, to identify any differences in the mechanism. It is important to identify as much as possible the redox steps as «fingerprints» present in the theoretical curve. The characteristics and possible assignments in the mechanical milling curve and in CuPBA F350 are summarized in Table 1 and Table 2 for the first and second cycle, respectively. This assignment of the electrochemical steps to FeF_3 or CuF_2 is based on their voltamograms presented in ESI and according to the literature (Tan et al. (Tan et al., 2014) for FeF_3 and Hua et al. (Hua et al., 2014) for CuF_2). The comparison of the theoretical curve with mechanical milling and CuPBA F350 is also presented in these tables.

The simple addition of the intensity of two components represents the electrochemical response in the absence of interactions between the redox centers. For the first cycle (Discharge (D) and Charge (C)), a larger peak intensity is observed for the milled sample compared to this theoretical curve.

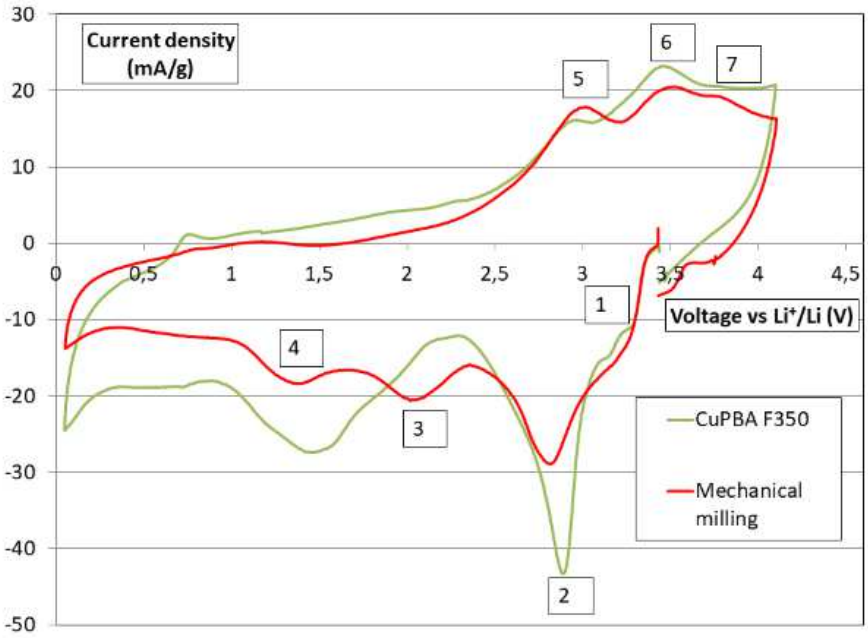

Figure 14: CV comparison of the 1st cycle of CuPBA F-350 and of sample obtained by ball milling of 3:2

CuF_2:FeF_3 ; Current obtained is corrected by the active mass and sweeping rate is 0.02 mV s^{-1}

Peak	Voltage range (V *vs.* Li^+/Li)	Redox events	Ball-milling	CuPBA F350
1	3.4-3.1 (D)	$FeF_3 + x\ Li^+ + e^- \rightarrow Li_xFeF_3$	+	+
2	3.1-2.6 (D)	$CuF_2 + 2\ Li^+ + 2\ e^- \rightarrow Cu + 2\ LiF$	+	++
3	1.8-1.5 (D)	$Li_xFeF_3 + (3\text{-}x)\ Li^+ + (3\text{-}x)\ e^- \rightarrow Fe + 3\ LiF$ One or two successive reactional steps	↗ +	↔ ++
4	1.4-1.2 (D)		+	
5	2.8-3.1 (C)	$Fe + 3\ LiF \rightarrow LixFeF_3 + (3\text{-}x)\ Li^+ + (3\text{-}x)\ e^-$	+	+
6	3.3-3.6 (C)	$Li_xFeF_3 \rightarrow FeF_3 + xLi^+ + xe^-$	+	+
7	3.7-3.9 (C)	$Cu + 2\ LiF \rightarrow CuF_2 + 2\ Li^+ + 2\ e^-$	+	+

Table 1: Redox identification in the first cycle from the theoretical curve and the associated assignment in ball-milled sample or CuPBA F350

Symbols for both tables: I: Intensity ; V: Voltage D: discharge, C: charge

Intensity: Equal intensity =, More intense +, very intense ++ ; Voltage: potential shift ↗ or , widening ↔

This confirms that the milling improves the redox activity of a physical addition of two-component CuF_2 and FeF_3. Discharge to 50 mV vs. Li^+/Li induces conversion of both cations and in turn electrochemical grinding of the active materials according to the redox events reported in Table 1. Interestingly, the ball-milling still presents overall higher intensity and voltages than the simple addition during the subsequent charging and the second cycle, confirming the improvement brought by multimetallic fluorinated composites over binary fluorides as cathodic materials.

The mechanism of CuPBA F350 and mechanical milling are then compared to highlight the differences between the two preparations of a multimetallic fluorinated nanocomposite. Comparing the voltamograms, the redox mechanisms are quite similar for both products, especially during the first charge and the second cycle. The benefits of multimetallic mixing over simple addition of the two metal fluorides are therefore retained with template fluorination and ball milling. Interestingly, striking differences are observed in the first reduction. For the CuF_2, the peak at 2.7 V is much more intense in CuPBA F350 than in mechanical milling. This may be due to a better dispersion of the redox centers obtained with the fluorination of CuPBA, leading to a reduction and homogenization

of the CuF_2 particle size compared to mechanical milling as observed by SEM previously, and thus improving the electrochemical activity of the copper. Better homogenization of CuF_2 and FeF_3 matrix is assessed by the SEM views analysis performed on CuPBA F350 and mechanical milling presented in Figure 11. Another interesting feature is the conversion step during the first discharge. The mechanical milling sample exhibits two relatively weak and separated peaks at 2.1 and 1.4 V while CuPBA F350 exhibits only one large and intense peak centered on 1.5 V. The latter results most likely from the merging of the doublet present in the mechanical milling product (labeled 3 and 4 in Table 1). This means that the conversion step which takes place in two separate steps for the milling product is different for CuPBA F350. It is possible that the transformations of intermediate phases during the conversion are facilitated in the case of CuPBA F350 compared to mechanical milling thanks again to the more homogeneous dispersion and size of the CuF_2 and FeF_3 domains assessed by SEM.

In oxidation, similar current densities are observed for CuPBA F350 and mechanical milling with a double peak related to the FeF_3 sample at 3 and 3.5 V followed by a peak at 3.8 V related to CuF_2 appearing as a weak peak also present in the theoretical curve at similar voltages.

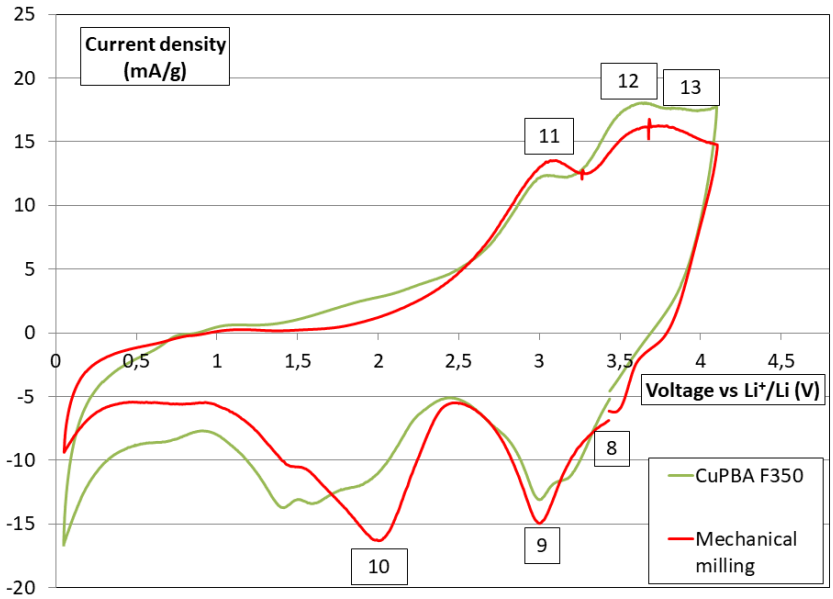

Figure 15: CV comparison of the 2nd cycle between CuPBA F-350 and product of mechanical milling of 3:2 CuF_2:FeF_3 ; Current obtained is corrected by the active mass and sweeping rate is 0.02 mV s^{-1}

Peak	Voltage range (V *vs*. Li^+/Li)	Redox events	Ball-milling	CuPBA F350
8	3.5-3.2 (D)	$CuF_2 + 2\ Li^+ + 2\ e^- \rightarrow Cu + 2\ LiF$	=	=
9	3.2-2.7 (D)	$FeF_3 + x\ Li^+ + x\ e^- \rightarrow LixFeF_3$	↔ ↗ +	↔ ↗ +
10	2.1-1.5 (D)	Conversion $LixFeF_3 + (3-x)\ Li^+ + (3-x)\ e^- \rightarrow Fe + 3\ LiF$	↗ ↔ +	↔ +
11	2.7-3.1 (C)	$Fe + 3\ LiF \rightarrow LixFeF_3 + (3-x)\ Li^+ + (3-x)\ e^-$	+	+
12	3.4-3.6 (C)	$LixFeF_3 \rightarrow FeF_3 + x\ Li^+ + x\ e^-$	+	+
13	3.7-3.9 (C)	$Cu + 2\ LiF \rightarrow CuF_2 + 2\ Li^+ + 2\ e^-$	+	+

Table 2: Redox identification in the second cycle from the theoretical curve and the associated assignment in ball-milled sample or CuPBA F350

For the second cycle, the CV shape is similar between the CuPBA F350 and ball milling samples. The threshold voltage of the conversion step appears to be slightly different with 2.4 V for mechanical milling and 2.3 V for CuPBA F350 but widens at a lower potential. Quantitatively, the improvement in the first discharge for template fluorination over mechanical milling stabilizes out in the second cycle, but both still present more interesting electrochemical properties than the simple addition of two components.

To approach a more practical use, galvanostatic measurements are performed in the voltage range 1 to 4.1 V. CuF_2 and FeF_3 are cycled under the same conditions as the references. The V(Q) profiles are shown in Figure 16 a) and the resulting dQ/dV derivative curves for the first discharge (1D) and charge (1C) are reported in Figure 16 b) and c) respectively. This allows the voltage of the associated electrochemical reactions to be compared (dQ/dV intensity is not taken into account here).

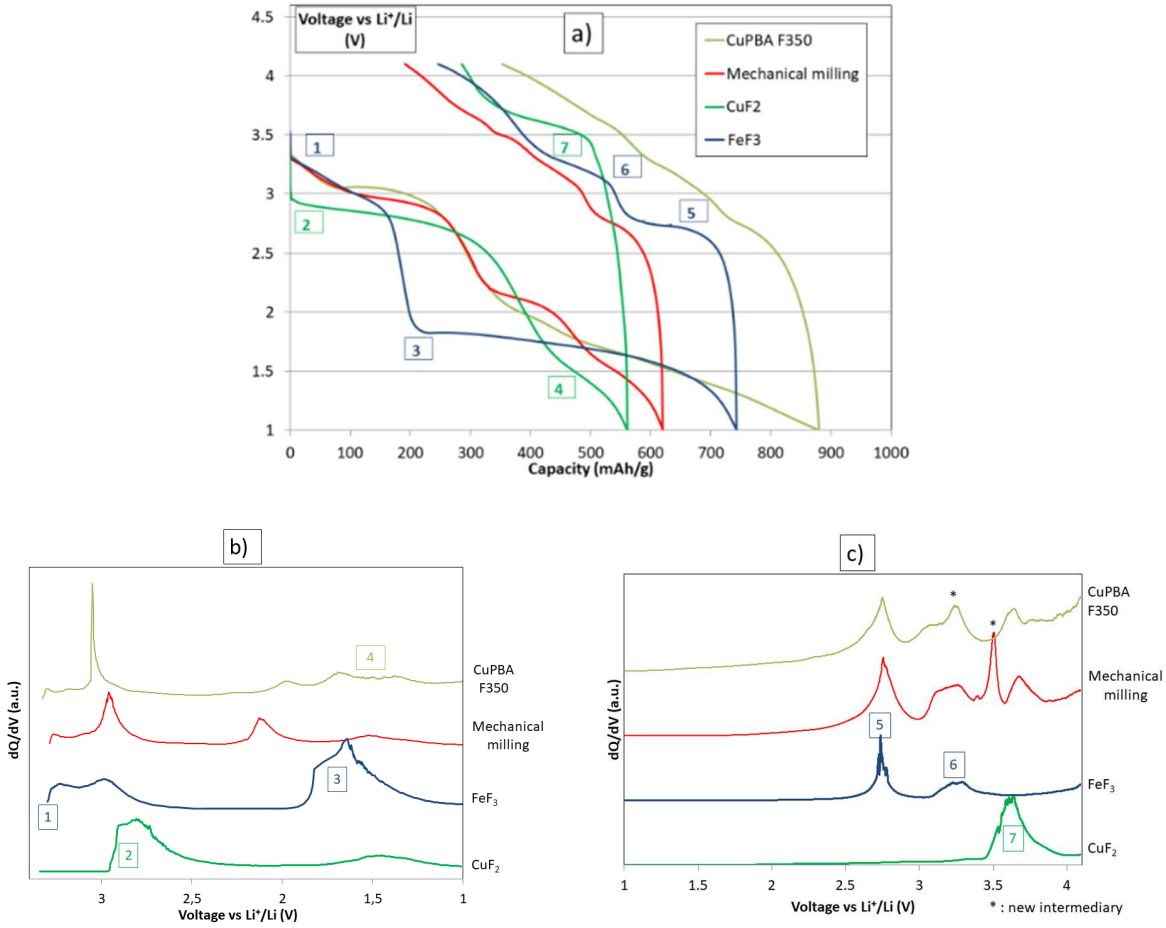

Figure 16: Profile in the first cycle (a) V(Q), b) dQ/dV (1D) and c) dQ/dV (1C)

Current density of 10 and 2 mA g^{-1} in 1D and 1C, respectively

In the case of FeF_3, CuF_2 and mechanical milling, the first discharge capacity Q(1D) reaches the theoretical maximum capacity with 714, 528 and 602 $mAh.g^{-1}$, respectively. This highlights the absence of side reactions of these fluorides with the PEO electrolyte and is in agreement with the CV analyses.

Q(1D) for CuPBA F350 is significantly higher than expected from its composition. An irreversible contribution may be behind this apparent increase in capacity such as an interaction between the solid polymer electrolyte and the fluorinated product.

During 1D, the average voltage for mechanical milling and CuPBA F350 is higher than for CuF_2 and FeF_3. This is in good agreement with the CV data which shows the advantage of the composite fluoride over the simple addition of its components, as shown in ESI.

Label	Voltage range (V vs. Li^+/Li)	Main Redox Event	Ball-milling	CuPBA F350
1	3.3-3.0	$FeF_3 + Li^+ + e^- \rightarrow LiFeF_3$	=	=
2	3.0-2.7	$CuF_2 + 2\ Li^+ + 2\ e^- \rightarrow Cu + 2\ LiF$	↗	↗↗
3	1.8-1.5	$LiFeF_3 + 2Li^+ + 2e^- \rightarrow Fe + 3\ LiF$	↗	↗
4	1.6-1.4	Interaction CuPBA F350/Solid polymer electrolyte	=	↗

Table 3: Summary of redox steps identified on the galvanostatic curves of CuF_2 and FeF_3 (Hua et al., 2021) and their derivative and comparison with CuPBA F350 and mechanical milling during the first discharge

Voltage: potential shift ↗, = or ↘

Label	Voltage range (V vs. Li^+/Li)	Main Redox Event	Ball milling	CuPBA F350
5	2.6-2.8	$Fe+3\ LiF \rightarrow LiFeF_3 + 2Li^+ + 2e^-$	=	=
6	3.1-3.3	$LiFeF_3 \rightarrow FeF_3 + Li^+ + e-$	↗	↘
*	3.2-3.5	New intermediary	3.5 V	3.2 V
7	3.4-3.7	$Cu+2LiF \rightarrow CuF_2 + 2\ Li^+ + 2\ e^-$	=	=

Table 4: Summary of redox steps identified on the galvanostatic curves of CuF_2 and r-FeF_3 and their derivative and comparison with CuPBA F350 and ball milling during the first charge

Voltage: potential shift ↗, = or ↘

It is known that redox events in the V(Q) galvanostatic mode are visualized by a plateau and a peak in the associated dQ/dV derivative curve. For ease of attribution, these contributions are labelled on the CuF_2 and FeF_3 curves. The characteristics of the different redox steps are summarized for 1D and 1C in Table 3 and in Table 4, respectively.

From the analysis of the V(Q) and dQ/dV profiles collected in the tables, the electrochemical mechanisms seem similar between CuPBA F350 and mechanical milling as already demonstrated by the CV analysis. Moreover, the 1D derivative curve analysis confirms higher reaction voltages than CuF_2 or FeF_3 alone and the improved electrochemical properties already assessed by CV. However, differences are detected between the two samples. A

plateau corresponding to the reduction of CuF_2 is located at 3.1 V in CuPBA F350 while the voltage drops for mechanical milling, showing the enhancement of the copper activity for the template fluorination as observed by CV.

Another interesting feature for CuPBA F350 is the conversion (< 2.1 V) with a smoother voltage evolution than with mechanical milling. This may be due to a better homogeneous dispersion of the redox centers as already indicated by CV. A more intimate mixing of the redox centers is expected to improve the synergy and therefore leads to the absence of clearly separated redox steps in the resulting galvanostatic curve, as observed in 1D by CV. The structure of CuPBA F350 favors interactions between the Cu and Fe redox centers, resulting in a more hybrid situation between each CuF_2 and FeF_3 mechanism, especially during conversion than after ball-milling.

During the following oxidation, the redox steps are difficult to represent because no clear plateau is observed anymore. The voltage of the redox reactions is compared by qualitatively analyzing the derived curve presented in Figure 16 c). The same three redox steps identified with FeF_3 (labelled 5 and 6) and CuF_2 (labelled 7) are maintained at the same voltage. However, an additional peak is present in both the derived 1C curve for CuPBA F350 and mechanical milling at 3.2 V for CuPBA F350 and 3.5 V for ball milling, marked with an asterisk. This additional peak could not be attributed to the redox of FeF_3 or CuF_2 and could therefore be due to the appearance of an additional intermediate phase in the electrochemical mechanism at the very low current density of 2 $mA.g^{-1}$ applied. It is interesting to note that this additional peak occurs at lower potential range for CuPBA F350 than for mechanical milling in 1C (maximum at 3.2 V versus 3.5 V): this reactional intermediate could therefore be easier to form in the case of CuPBA F350 than in the product of mechanical milling thanks to a better homogeneous dispersion and regular size of the redox domains.

This electrochemical study confirms the relevance of MMTF (Multi Metallic Template Fluorination) method for the preparation of multi-metallic fluorinated composites as cathode materials in Li solid state batteries. This method has a major advantage in terms of scalability compared to ball milling but also induces a better dispersion and regular size of the redox domains in the formed composite leading to slightly better electrochemical properties as evaluated by CV and galvanostatic measurements.

A long cycle study could help confirm whether this first cycle improvement has an impact on capacity retention or voltage hysteresis. Results beyond the first discharge presented in this article are not directly comparable with the

literature in terms of capacity or current density as the coin cell assembly used does not promote cyclability and was used to unravel differences in the mechanism. However, it can be noted that the first galvanostatic discharge for the mechanical milling product is rather similar to results obtained by Wang et al. on a $Cu_xFe_{1-x}F_2$ material with two plateaus at 3 V and 2.2 V at similar capacity values. Therefore, CuPBA F350 could perform better than this literature reference on prolonged cycling in similar conditions. This long cycle study could confirm improvement brought by MMTF over mechanical milling products observed in literature in terms of electrochemical performances additionally to the improvement brought by the solid gas fluorination synthesis method.

Moreover, some works are needed to reduce the polarization by optimizing electrode formulation, porosity and weight. Such works are on progress.

4. Conclusion

CuPBA is chosen as a template for fluorination for its multi-metallic structure, fluorine-substitutable cyanide ligands and its open structure that favours fluorine diffusion for an optimal reaction. Moreover, it is easily synthesized in stoichiometric quantities by a simple co-precipitation protocol. A thermal study highlights the successive structural modifications occurring under air, showing the possibility of maintaining the structure of the model up to 170 °C while oxides are formed at 350 °C. Based on this, fluorination temperatures are selected. The combined XAS and XRD analyses confirm the possibility of obtaining different structures by adjusting the fluorination temperature. At low temperatures, an anti-perovskite phase $[Cu(H_2O)_4]_3.(FeF_6)_2$ is obtained, showing that a multi-metallic fluorinated structure is maintained after fluorination of CuPBA. After a severe change in local order identified by XAS at 200 °C and especially around copper cations, fluorination leads to CuF_2 and HTB-FeF_3 phases at 350 °C.

The electrochemical properties of CuPBA fluorination products are investigated by CV and in galvanostatic mode with a solid electrolyte membrane It is found that the fluorinated CuPBA at 350°C performs slightly better than the mechanical milling reference, and both much better than the simple addition of its two components, CuF_2 and FeF_3. This is due to an even more pronounced homogeneous initial dispersion of the Cu and Fe redox centres in CuPBA F350 than in the blank model and even than the milling reference as assessed by coupled SEM/EDX mapping analyses.

Moreover, some works are needed to reduce the polarization by optimizing electrode formulation, porosity and weight. Such works are on progress.!

The Multi Metallic Template Fluorination (MMTF) strategy detailed in this article and based on the preliminary thermal evolution mechanism study of the inorganic template should be generalized to a large variety of Metal Organic Frameworks or multifunctional compounds such as Layered Double Hydroxides. We believe that this strategy combining molecular fluorination with MMT opens the possibility of forming multiple structures and morphologies of fluorides of potential interest for different applications, such as cathodic materials on a large scale in our case.

5. ACKNOWLEDGMENTS

We acknowledge Synchrotron SOLEIL for provision of synchrotron radiation facilities, and we would like to thank A. Zitolo for assistance in using beamline SAMBA and S Belin for XAS interpretation. We also thank N. Demarthe and B. Cluzeau for assisting in XAS measurements.

6. REFERENCES

Batisse, N., Guérin, K., Dubois, M., & Hamwi, A. (2011). The synthesis of microporous carbon by the fluorination of titanium carbide. *Carbon*, *49*(9), 2998-3009. https://doi.org/10.1016/j.carbon.2011.03.018

Belli, M., Scafati, A., Bianconi, A., Mobilio, S., Palladino, L., Reale, A., & Burattini, E. (1980). X-ray absorption near edge structures (XANES) in simple and complex Mn compounds. *Solid State Communications*, *35*(4), 355-361. https://doi.org/10.1016/0038-1098(80)90515-3

Briois, V., Fonda, E., Belin, S., Barthe, L., La Fontaine, C., Langlois, F., Ribbens, M., & Villain, F. (2011). SAMBA : The 4–40 keV X-ray absorption spectroscopy beamline at SOLEIL. *UVX 2010 - 10e Colloque sur les Sources Cohérentes et Incohérentes UV, VUV et X ; Applications et Développements Récents*, 41-47. https://doi.org/10.1051/uvx/2011006

Cheng, M., Liu, Y., Huang, D., Lai, C., Zeng, G., Huang, J., Liu, Z., Zhang, C., Zhou, C., Qin, L., Xiong, W., Yi, H., & Yang, Y. (2019). Prussian blue analogue derived magnetic Cu-Fe oxide as a recyclable photo-Fenton catalyst for the efficient removal of sulfamethazine at near neutral pH values. *Chemical Engineering Journal*, *362*, 865-876. https://doi.org/10.1016/j.cej.2019.01.101

de Tacconi, N. R., Rajeshwar, K., & Lezna, R. O. (2003). Metal Hexacyanoferrates : Electrosynthesis, in Situ Characterization, and Applications. *Chemistry of Materials*, *15*(16), 3046-3062. https://doi.org/10.1021/cm0341540

Doebelin, N., & Kleeberg, R. (2015). *Profex* : A graphical user interface for the Rietveld refinement program *BGMN*. *Journal of Applied Crystallography*, *48*(5), 1573-1580. https://doi.org/10.1107/S1600576715014685

Farges, F., Brown, G. E., & Rehr, J. J. (1997). Ti K -edge XANES studies of Ti coordination and disorder in oxide compounds : Comparison between theory and experiment. *Physical Review B*, *56*(4), 1809-1819. https://doi.org/10.1103/PhysRevB.56.1809

Gu, X., Liu, Z., Liu, H., Pei, C., & Feng, L. (2021). Fluorination of ZIF-67 framework templated Prussian blue analogue nano-box for efficient electrochemical oxygen evolution reaction. *Chemical Engineering Journal*, *403*, 126371. https://doi.org/10.1016/j.cej.2020.126371

Hayner, C. M., Zhao, X., & Kung, H. H. (2012). Materials for Rechargeable Lithium-Ion Batteries. *Annual Review of Chemical and Biomolecular Engineering*, *3*(1), 445-471. https://doi.org/10.1146/annurev-chembioeng-062011-081024

Hua, X., Eggeman, A. S., Castillo-Martínez, E., Robert, R., Geddes, H. S., Lu, Z., Pickard, C. J., Meng, W., Wiaderek, K. M., Pereira, N., Amatucci, G. G., Midgley, P. A., Chapman, K. W., Steiner, U., Goodwin, A. L., & Grey, C. P. (2021). Revisiting metal fluorides as lithium-ion battery cathodes. *Nature Materials*. https://doi.org/10.1038/s41563-020-00893-1

Hua, X., Robert, R., Du, L.-S., Wiaderek, K. M., Leskes, M., Chapman, K. W., Chupas, P. J., & Grey, C. P. (2014). Comprehensive Study of the CuF_2 Conversion Reaction Mechanism in a Lithium Ion Battery. *The Journal of Physical Chemistry C*, *118*(28), 15169-15184. https://doi.org/10.1021/jp503902z

Huang, Q., Turcheniuk, K., Ren, X., Magasinski, A., Song, A.-Y., Xiao, Y., Kim, D., & Yushin, G. (2019). Cycle stability of conversion-type iron fluoride lithium battery cathode at elevated temperatures in polymer electrolyte composites. *Nature Materials*, *18*(12), 1343-1349. https://doi.org/10.1038/s41563-019-0472-7

Ju, H., Liu, X. D., Tao, C. Y., Yang, F., Liu, X. L., Luo, X., & Zhang, L. (2021). Prussian blue analogue derived low-crystalline Mn2O3/Co3O4 as high-performance supercapacitor electrode. *Journal of Alloys and Compounds*, *856*, 157134. https://doi.org/10.1016/j.jallcom.2020.157134

Kummer, S., & Babel, D. (1987). Die anti-perowskitartige Kristallstruktur von Tris[tetraquokupfer(II)]-bis[hexafluorometallaten(III)], Cu3M2F12·12H2O (M = V, Cr, Fe) / The anti-Perovskite-Like Crystal Structure of Tris[tetraquocopper(II)]-bis[hexafluorometallates(III)], Cu3M2F12 · 12H2O (M = V, Cr, Fe). *Zeitschrift für Naturforschung B*, *42*(11), 1403-1410. https://doi.org/10.1515/znb-1987-1107

Lemoine, K., Moury, R., Durand, E., Dompablo, E. A., Morán, E., Leblanc, M., Hémon-Ribaud, A., Grenèche, J.-M., Galven, C., Gunes, V., Lhoste, J., & Maisonneuve, V. (2021). First Mixed-Metal Fluoride Pyrochlores Obtained by Topotactic Oxidation of Ammonium Fluorides under F_2 Gas. *Crystal Growth & Design*, *21*(2), 935-945. https://doi.org/10.1021/acs.cgd.0c01279

Lemoine, K., Zhang, L., Dambournet, D., Grenèche, J.-M., Hémon-Ribaud, A., Leblanc, M., Borkiewicz, O. J., Tarascon, J.-M., Maisonneuve, V., & Lhoste, J. (2019). Synthesis by Thermal Decomposition of Two Iron Hydroxyfluorides : Structural Effects of Li Insertion. *Chemistry of Materials*, *31*(11), 4246-4257. https://doi.org/10.1021/acs.chemmater.9b01252

Lemoine, K., Zhang, L., Grenèche, J.-M., Hémon-Ribaud, A., Leblanc, M., Guiet, A., Galven, C., Tarascon, J.-M., Maisonneuve, V., & Lhoste, J. (2019). New Amorphous Iron-Based Oxyfluorides as Cathode Materials for High-Capacity Lithium-Ion Batteries. *The Journal of Physical Chemistry C*, *123*(35), 21386-21394. https://doi.org/10.1021/acs.jpcc.9b06055

Li, Y., Hu, J., Yang, K., Cao, B., Li, Z., Yang, L., & Pan, F. (2019). Synthetic control of Prussian blue derived nano-materials for energy storage and conversion application. *Materials Today Energy*, *14*, 100332. https://doi.org/10.1016/j.mtener.2019.07.003

Martínez-Garcia, R., Knobel, M., & Reguera, E. (2006). Thermal-Induced Changes in Molecular Magnets Based on Prussian Blue Analogues. *The Journal of Physical Chemistry B*, *110*(14), 7296-7303. https://doi.org/10.1021/jp0555551

Nitta, N., Wu, F., Lee, J. T., & Yushin, G. (2015). Li-ion battery materials : Present and future. *Materials Today*, *18*(5), 252-264. https://doi.org/10.1016/j.mattod.2014.10.040

Ojwang, D. O., Grins, J., Wardecki, D., Valvo, M., Renman, V., Häggström, L., Ericsson, T., Gustafsson, T., Mahmoud, A., Hermann, R. P., & Svensson, G. (2016). Structure Characterization and Properties of K-Containing Copper Hexacyanoferrate. *Inorganic Chemistry*, *55*(12), 5924-5934. https://doi.org/10.1021/acs.inorgchem.6b00227

Pattrick, R. A. D., Mosselmans, J. F. W., Charnock, J. M., England, K. E. R., Helz, G. R., Garner, C. D., & Vaughan, D. J. (1997). The structure of amorphous copper sulfide precipitates : An X-ray absorption study. *Geochimica et Cosmochimica Acta*, *61*(10), 2023-2036. https://doi.org/10.1016/S0016-7037(97)00061-6

Ravel, B., & Newville, M. (2005). *ATHENA* , *ARTEMIS* , *HEPHAESTUS* : Data analysis for X-ray absorption spectroscopy using *IFEFFIT*. *Journal of Synchrotron Radiation*, *12*(4), 537-541. https://doi.org/10.1107/S0909049505012719

Rozier, P., & Tarascon, J. M. (2015). Review—Li-Rich Layered Oxide Cathodes for Next-Generation Li-Ion Batteries : Chances and Challenges. *Journal of The Electrochemical Society*, *162*(14), A2490-A2499. https://doi.org/10.1149/2.0111514jes

Tan, H. J., Smith, H. L., Kim, L., Harding, T. K., Jones, S. C., & Fultz, B. (2014). Electrochemical Cycling and Lithium Insertion in Nanostructured FeF3 Cathodes. *Journal of the Electrochemical Society*, *161*(3), A445-A449. https://doi.org/10.1149/2.096403jes

Villa, C., Kim, S., Lu, Y., Dravid, V. P., & Wu, J. (2019). Cu-Substituted NiF_2 as a Cathode Material for Li-Ion Batteries. *ACS Applied Materials & Interfaces*, *11*(1), 647-654. https://doi.org/10.1021/acsami.8b15791

Wang, D., Lv, H., Hussain, T., Yang, Q., Liang, G., Zhao, Y., Ma, L., Li, Q., Li, H., Dong, B., Kaewmaraya, T., & Zhi, C. (2021). A manganese hexacyanoferrate framework with enlarged ion tunnels and two-species redox reaction for aqueous Al-ion batteries. *Nano Energy*, *84*, 105945. https://doi.org/10.1016/j.nanoen.2021.105945

Wang, F., Kim, S.-W., Seo, D.-H., Kang, K., Wang, L., Su, D., Vajo, J. J., Wang, J., & Graetz, J. (2015). Ternary metal fluorides as high-energy cathodes with low cycling hysteresis. *Nature Communications*, *6*(1), 6668. https://doi.org/10.1038/ncomms7668

Wessells, C. D., Peddada, S. V., McDowell, M. T., Huggins, R. A., & Cui, Y. (2011). The Effect of Insertion Species on Nanostructured Open Framework Hexacyanoferrate Battery Electrodes. *Journal of The Electrochemical Society*, *159*(2), A98-A103. https://doi.org/10.1149/2.060202jes

Wilke, M., Farges, F., Petit, P.-E., Brown, G. E., & Martin, F. (2001). Oxidation state and coordination of Fe in minerals : An Fe *K*- XANES spectroscopic study. *American Mineralogist*, *86*(5-6), 714-730. https://doi.org/10.2138/am-2001-5-612

Wu, F., Maier, J., & Yu, Y. (2020). Guidelines and trends for next-generation rechargeable lithium and lithium-ion batteries. *Chemical Society Reviews*, *49*(5), 1569-1614. https://doi.org/10.1039/C7CS00863E

Zhang, L., Wu, H. B., & Lou, X. W. (David). (2013). Metal–Organic-Frameworks-Derived General Formation of Hollow Structures with High Complexity. *Journal of the American Chemical Society*, *135*(29), 10664-10672. https://doi.org/10.1021/ja401727n

Zhang, L., Wu, H. B., Madhavi, S., Hng, H. H., & Lou, X. W. (David). (2012). Formation of Fe_2O_3 Microboxes with Hierarchical Shell Structures from Metal–Organic Frameworks and Their Lithium Storage Properties. *Journal of the American Chemical Society*, *134*(42), 17388-17391. https://doi.org/10.1021/ja307475c

.

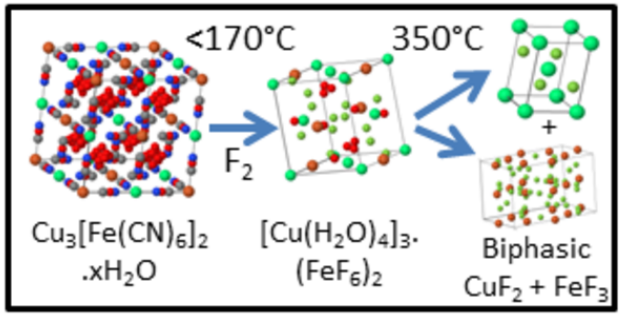
<170°C
350°C
F2
+
Cu3[Fe(CN)6]2
.xH2O
[Cu(H2O)4]3.
(FeF6)2
Biphasic
CuF2 + FeF3